


 Cite this: *RSC Adv.*, 2020, 10, 21180

Investigation of the effect of S/In molar ratio on physical properties of sprayed In_2S_3 thin films

 Y. Bchiri,^a N. Bouguila,^{ID}*^a M. Kraini,^a R. Souissi,^{bc} C. Vázquez-Vázquez,^{ID}^d M. A. López-Quintela,^{ID}^d and S. Alaya^a

Indium sulfide (In_2S_3) thin films have been synthesized on glass substrates using the spray technique (CSP). The S : In molar ratio was varied from 1 to 4 in the starting solution. The Raman analysis confirms the formation of the $\beta\text{-In}_2\text{S}_3$ material and the absence of a secondary phase. The EDS analysis reveals that our layers are pure. The thin film surface is free of cracks, as observed in AFM images. Optical transmission achieved 80% in the visible and near infrared region. The refractive index (n) is affected by the changes in the S/In molar ratio. The optical parameters, single oscillator energy (E_0), dispersion energy (E_d) and high frequency dielectric constant (ϵ_∞), are calculated *via* the Wemple–DiDomenico model. In addition, the photoconductivity kinetics in In_2S_3 films for S/In = 2 were investigated and analyzed. The I – V characteristics and the photoresponse were also studied.

 Received 31st March 2020
 Accepted 27th May 2020

DOI: 10.1039/d0ra02945a

rsc.li/rsc-advances

1. Introduction

Most promising sulfide based semiconductor materials have been used as light absorbers in solar cells such as chalcopyrite CuInS_2 , paramagnetic insulator $\text{Fe}_{1-x}\text{Co}_x\text{S}_2$, antimony sulfide Sb_2S_3 and sulfide indium In_2S_3 . The thermodynamic efficiency of various devices is of wide interest because of the relevance of this parameter for energy conversion.

The efficiency of MEH-PPV/H-CuInS₂ hybrid solar cells was studied by Yue *et al.*¹ Hierarchical CuInS_2 was deposited with the induction of histidine by solvothermal method. The authors found that devices based on H-CuInS₂ synthesized with smaller size (0.5 HD) displayed higher energy conversion efficiency of 0.59%. The chalcopyrite CuInS_2 quantum dots (CuInS_2 -QDs) with different sizes synthesized by the solvothermal method was used in MEH-PPV– $\text{CuInS}_2/\text{TiO}_2$ -NA solar cells.² The authors obtained a peak efficiency of 1.60% for the 5.4 nm CuInS_2 -QDs. In addition, this efficiency is comparable to the QDSSCs based on CdS sensitized TiO_2 -NA.³

Recently, a series of $\text{Fe}_{1-x}\text{Co}_x\text{S}_2$ ($x = 0$ – 0.5) solid solutions have been synthesized and served as counter electrodes in dye sensitized solar cells (DSSCs).⁴ The results reveal high power conversion efficiency of 8.36% than those solid solutions

materials over Pt of 7.66%. Wu *et al.*⁵ studied hybrid $\text{TiO}_2/\text{Sb}_2\text{S}_3/\text{P3HT}$ n–i–p solar cells with Sb_2S_3 layers of different thickness by CBD method. They reported an optimum efficiency of 1.65% with Sb_2S_3 thickness of 175 nm.

However, the use of cadmium (Cd) in PV devices is undesirable from the viewpoint of environmental safety,⁶ serious efforts have been made to substitute the CdS by other non-toxic (Cd-free). Indium sulfide (In_2S_3) is one of the possible candidates to replace CdS a buffer layer. This compound is an n-type semiconductors which belongs to III–VI group. Hetro-juncture such as CIGS/ $\beta\text{-In}_2\text{S}_3$ (ref. 7) achieved a conversion efficiencies of 15.7%. This demonstrates that comparable conversion efficiencies can be obtained respect to commonly used CdS buffer (16%).⁸ Osman *et al.*⁹ observed that there is no difference between both structures of CdS and In_2S_3 , they found also that the efficiency of CIGS solar cells with both layers is comparable. It's 24.14% and 24.28% with In_2S_3 and CdS respectively.

In_2S_3 is currently researched as a result of its important properties in relation with the optoelectronic devices.¹⁰ $\beta\text{-In}_2\text{S}_3$ is recognized as a direct band gap semiconductor ranging from 2.0 to 2.75 eV, with a high stability, high optical transmittance (>80%) and controllable electrical properties, modified chemical composition and deposition parameters.^{11,12} These characteristics of In_2S_3 films make it a useful material for several applications. In_2S_3 can be used in light-emitting diode (LED) and lithium-ion batteries.^{13,14} Due to its absorption in the UV and visible region, In_2S_3 is considered as photodetector.¹⁵ Also, this material can be used for gas sensing and photocatalytic applications owing to its thermal stability, good response and reversibility, low defect density and simple synthesis process.^{16,17}

^aLaboratoire de Physique des Matériaux et des Nanomatériaux appliquée à l'Environnement, Faculté des Sciences, Université de Gabès, Cité Erriadh Manara Zrig, 6072, Gabès, Tunisia. E-mail: nour.bouguila@fsg.rnu.tn

^bTunis University, Ecole Nationale Supérieure d'ingénieurs de Tunis (ENSIT), Tunisia

^cUniversité de Carthage, Laboratoire des Matériaux, Molécules et Applications IPEST, BP 51, La Marsa 2070, Tunis, Tunisia

^dLaboratory of Magnetism and Nanotechnology (NANOMAG), Department of Physical Chemistry, Faculty of Chemistry, Universidade de Santiago de Compostela, 15782 Santiago de Compostela, Spain



In_2S_3 exists in three different crystalline phases α , β and γ which depend on the growth temperature.^{12,18} $\beta\text{-In}_2\text{S}_3$ is the most stable phase at room temperature.^{19,20} It crystallizes in a defect spinel structure with a high degree of tetrahedral and octahedral vacancy sites.^{21,22}

Various techniques were commonly used for preparing In_2S_3 , such as spray pyrolysis,^{23,24} ultrasonic dispersion,²⁵ physical vapor deposition,²⁶ chemical bath deposition,²⁷ vacuum thermal evaporation,²⁸ *etc.* Among these methods, the spray pyrolysis technique is of particular interest because it is economical and allows growing large area In_2S_3 thin films. Furthermore, this technique has been applied to fabricate various type of materials such as ZnO and carbon nanofibres (ECN/ TiO_2).^{29,30} Indeed, Ngo *et al.*³⁰ presented a comparative study between ZnO films deposited by spray coating and ZnO prepared by spin coated. They found that the spray coated sample have higher efficiency (3.76%) than spin coated ZnO (3.11%) due to the increase in FF from 42.38% to 63.14%. So that, to choice of technique is one of important factor in solar cells application.

The physical properties of In_2S_3 thin films are strongly affected by the deposition parameters.²⁵ Several authors have reported that 340 °C is a good substrate temperature for obtaining best crystallinity.^{31,32} Thus, various works showed that the S/In ratio has an effect on the structure, the crystallite

size^{33–35} and the optical band gap of the In_2S_3 films.^{11,36} Zhang *et al.*³⁷ have reported that the grain size increases from 32 nm to 34.1 nm with the increase of S/In molar ratio from 1 to 4. Furthermore, the high transmittance is found in the visible and near-infrared range. The energy band gap increases significantly when S/In ratio varies from 1 to 2, then decreases from 2.46 eV to 2.4 eV when S/In increases from 2 to 4. John *et al.*¹¹ have reported that the use of sulfur-rich solution (S/In = 8/2 instead of S/In = 2/1) decreases the energy band gap from 2.81 to 2.64 eV. The photoluminescence (PL) properties of In_2S_3 at different S/In ratios have been reported by Elfarrass *et al.*³³ They showed that all the films have two emission bands (green and red band). In addition, Bhira *et al.*³⁸ have demonstrated that In_2S_3 thin film has high photoconductivity. Therefore, investigations on the effect of S/In ratio on the In_2S_3 optical properties are very important, to obtain films that are capable to ensure stable and high efficient devices.

In this work, we report the study of the effect of S/In ratio on the physical properties of In_2S_3 thin films.

2. Experimental details

In_2S_3 thin films were produced by spray pyrolysis method using an aqueous solution of indium chloride(III) and thiourea, on glass substrate. The concentration of the precursor InCl_3 is

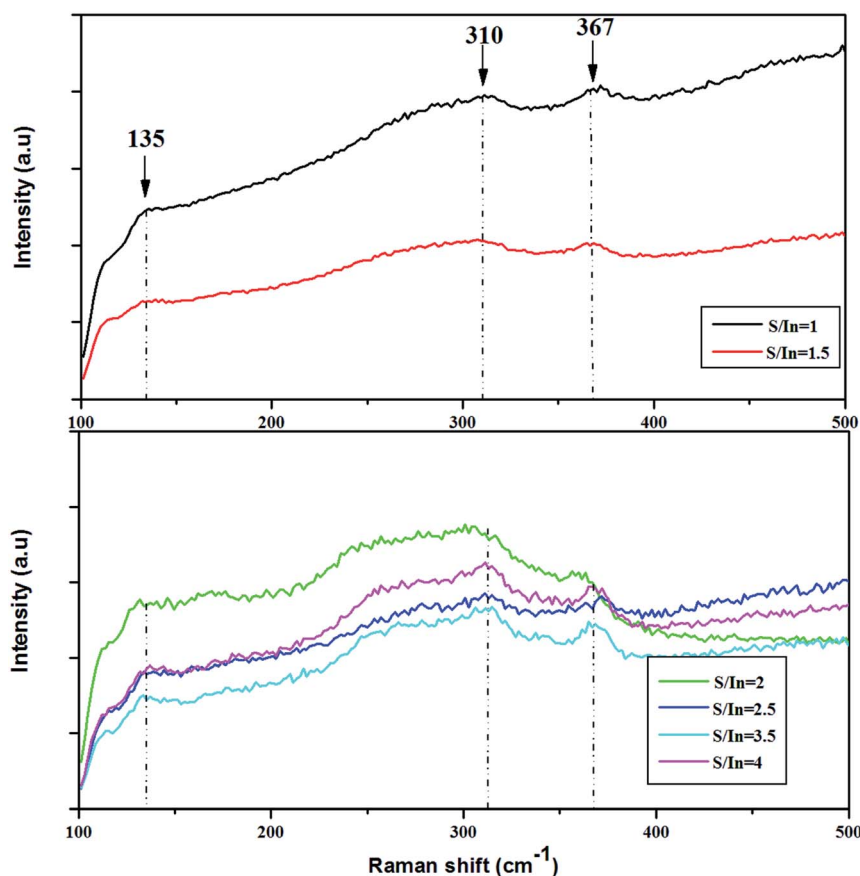
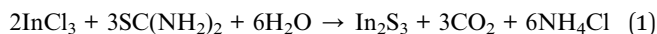


Fig. 1 Raman spectra of In_2S_3 thin films for different S/In molar ratios.



10^{-2} mol L $^{-1}$. The S/In ratio in the solution varied in the range 1–4. The substrate temperature was fixed at 340 °C within an accuracy of ± 5 °C, in agreement with^{31,32}. Compressed nitrogen was used as a carrier gas at a flow rate of 6 L min $^{-1}$.

The formation of In₂S₃ results from the following endothermic reaction:



The Raman analysis were conducted using a Jobin-Yvon microRaman spectrometer (T64000) with an argon laser line of 514 nm. The composition of films was done by energy dispersive spectroscopy (EDS). The surface morphology was performed by atomic force microscopy using an XE-100 instrument (Park Systems Corporation). Photoluminescence (PL) measurements were performed at room temperature using laser excitation wavelength of 655 nm. Transmittance spectra measurements have been done using a Shimadzu UV 3101 PC spectrophotometer in the wavelength range from 350 to 1900 nm. The *I*-*V* characteristics measured in dark and under illumination were performed using a (HP4140B) source/picoammeter. Moreover, the photoresponse of In₂S₃ thin films was investigated by illuminating the film with a neon light

source. The resistance of the sample is measured by using a (HP4140B) Keithley Digital multimeter, interfaced to a computer for data acquisition.

3. Results and discussion

3.1. Structural characterization

The quality of sprayed films was characterized by Raman spectroscopy. It's a powerful technique which allows to determine the phase and the structure of films. Besides, this technique provides the information about the vibration mode in the crystalline phase. The Raman spectra for our films are presented in Fig. 1, which were recorded in the energy region between 100 and 500 cm $^{-1}$. All the spectra reveal broad bands at 135, 310 and 367 cm $^{-1}$ with low intensity, showing nano-crystalline nature of the layers. These present bands seem to be typical relative to cubic structural (β -In₂S₃).^{39,40} The peak at 135 cm $^{-1}$ can be assigned to the E_g mode, and the peaks at 310, 367 cm $^{-1}$ to the A_{1g} mode.^{40–42} The band appeared at 310 cm $^{-1}$ is related to the symmetric stretching vibrating mode of InS₄ tetrahedral.⁴³ Furthermore, the shift in the position of the bands with molar ratio S/In could be due to the presence of strain developed in the films. The shift is in order of 2 cm $^{-1}$.

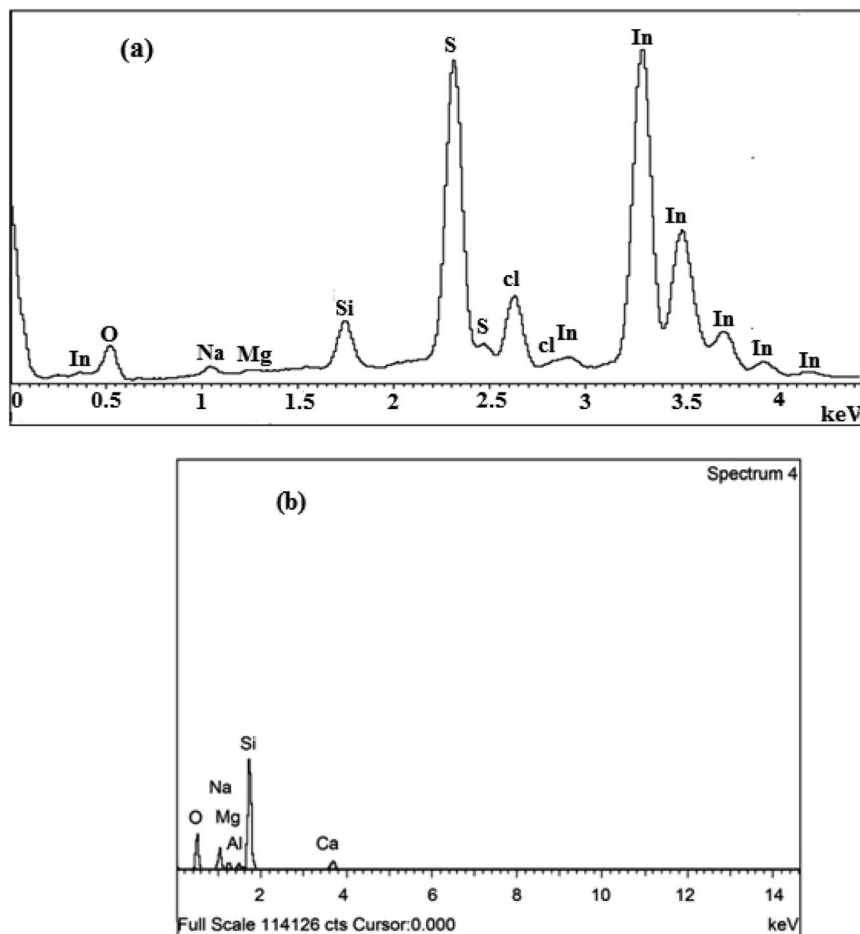


Fig. 2 (a) EDS spectra of thin films at different S/In molar ratios. (b) EDX spectrum of glass substrate.⁴⁵



Table 1 Chemical composition of In_2S_3 films

S/In	S (at%)	In (at%)	S/In
1	24.60	25.01	0.98
1.5	52.18	42.34	1.23
2	41.93	33.51	1.24
2.5	46.92	36.76	1.27
3.5	41.02	32.08	1.28
4	41.02	32.08	1.28

This induces the deviation in the interplanar spacing in crystal lattice. The change of S/In ratio does not affect the structure of the layers. In addition, we noticed the absence of secondary phases in the all layers. This finding proved the results obtained by XRD analysis.⁴⁴

3.2. EDS analysis

The compositional analysis of In_2S_3 thin films at different S/In molar ratios was carried out employing EDS as shown in Fig. 2a and Table 3. The EDS spectrum confirms the presence of

Table 2 Evolution of RMS roughness of In_2S_3 films with different S/In molar ratios

S/In	1	1.5	2	2.5	3.5	4
RMS (nm)	20	15	11	9	8	6

In and S elements in the films, their atomic percentages are given in Table 1. It can be seen that when the S/In increases in the solution, the S/In in the films increases and varies from 0.98 to 1.29. The Cl peak arises from the InCl_3 precursor. Also, we notice the presence of various elements such as Si, O, Na and Mg which are provided from glass substrates (see Fig. 2b).⁴⁵ Therefore, the EDS analysis confirms the purity of deposited In_2S_3 thin films.

3.3. Morphological characterization

Fig. 3a shows 2D and 3D NC-AFM images ($2\ \mu\text{m} \times 2\ \mu\text{m}$) of In_2S_3 films for S/In ratios equal to 1, 2 and 4. As observed from the AFM images, the surface morphology of the films is sensitive to the S/In molar ratio. Indeed, it can be seen that the films are formed by grains separated by depressions. Owing to the

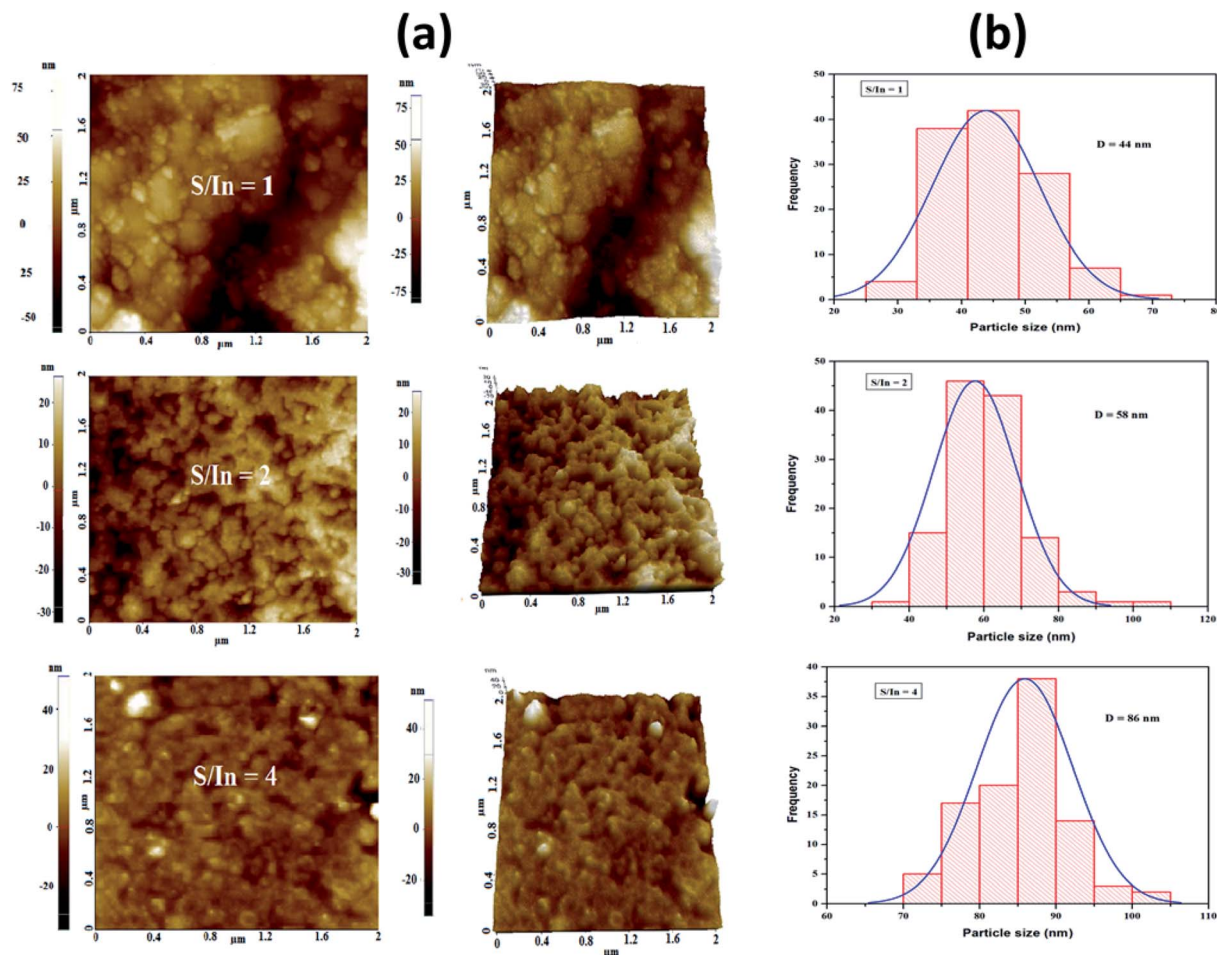


Fig. 3 (a) 2D and 3D NC-AFM images of thin films for S/In molar ratios equal to 1, 2 and 4. (b) Grain size distribution histogram of thin films for S/In molar ratios equal to 1, 2 and 4.



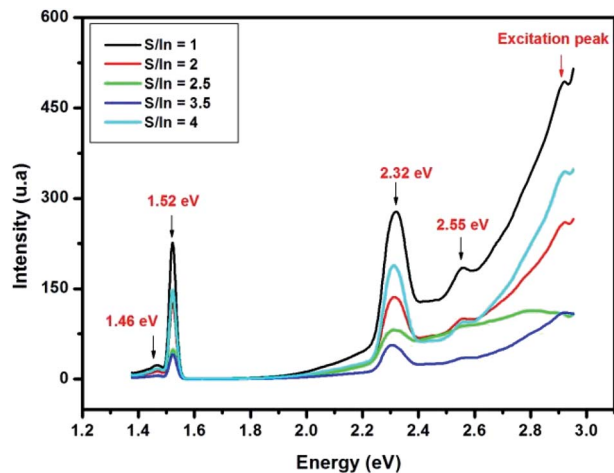


Fig. 4 Photoluminescence spectra of In_2S_3 thin films for different S/In molar ratios.

coalescence phenomenon, it appears that the grain size along the surface of the film increases with S/In ratio. Furthermore, we can note also that the films show spherical grains, indicating the polycrystalline nature of these films. This finding agrees with the XRD results. The root mean square roughness (RMS) values decrease from 20 to 6 nm with increasing molar ratio (Table 2). This behavior can be attributed to the increase of crystallite size, and the surface morphology becomes uniform and more compact.

In order to evaluate the average grain size, a statistical count of grain size was performed on the AFM images using Image-J software. Grain size distribution histograms for the different films are shown in Fig. 3b. The average grain size of samples is found to lie in the nanometer range (44–86 nm).

3.4. Optical characterization

3.4.1. Photoluminescence. The photoluminescence (PL) analysis was performed out for all the deposited In_2S_3 thin films at the excitation wavelength $\lambda = 655$ nm to investigate the defect state emission in the films.

Room temperature photoluminescence spectra of In_2S_3 at different S/In molar ratios are exhibited in Fig. 4. PL spectra reveal a peak at 1.46 eV, 1.52 eV, 2.32 eV and 2.55 eV.

The red emission at 1.45 is due to S and In vacancies in the host lattice.⁴⁶ The emission at 1.52 eV and green emission (at 2.32 eV and 2.55 eV) are attributed to transitions from the excited states of the sulfur vacancy (V_S) to the In vacancy (V_{In}) level.^{46–48} Mathew *et al.*²² reported a green emission from In_2S_3 which was attributed to the donor level formed by indium interstitials. The PL emission intensity is found stranger for sample at S/In = 1 than other samples, which proved the presence of higher defect concentration.⁴⁹ Thus, the emission intensity decreased indicated the reduction of defects in films. The low emission intensity is obtained for sample at S/In = 3,5, which the crystallinity is the best one. The same result was reported by Ajili *et al.*⁵⁰

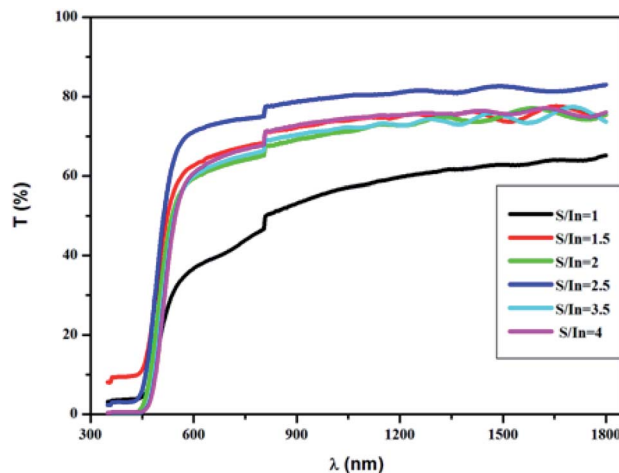


Fig. 5 Transmittance spectra with different S/In molar ratios.

In addition, the last peak at 2.55 eV is relative to the E_g values estimated from Tauc formula in earlier work by Bouguila *et al.*⁴⁴

3.4.2. Transmittance spectra. Fig. 5 gives the variation of the transmittance (T) spectra of In_2S_3 films. It is clear from Fig. 5 that the transmittance is improved with S/In molar ratio and it exceeds 80% in the visible and near infrared regions. Its increase until S/In = 2.5 may be related to the crystallinity improvement. Besides, we obtained a low transmittance at the molar ratio S/In = 1. This can be explained by two reasons: the high surface roughness and the stoichiometric deviation. Indeed, the transmittance is highly sensitive to the distribution of grains and their height variation on the layer surface.⁵¹ We notice out the presence of interference fringes in the transmittance spectra, showing the good uniformity and homogeneity of these films. In addition, we observe a sharp signal drop near the band edge due to the presence of direct transitions in the samples,⁵² also, this result is obtained in a previous publication by Bouguila *et al.*⁴⁴ Besides, two regions in the transmittance spectra are clearly noted: the first region, of a strong absorption ($\lambda < 570$ nm), is the fundamental absorption in the film due to the interband electronic transition. This region allows us to obtain the energy gap (E_g). The second region is of high transparency ($\lambda > 570$ nm). One can also observe that all the films are opaque in UV region. Therefore, these films can be used as UV detectors.

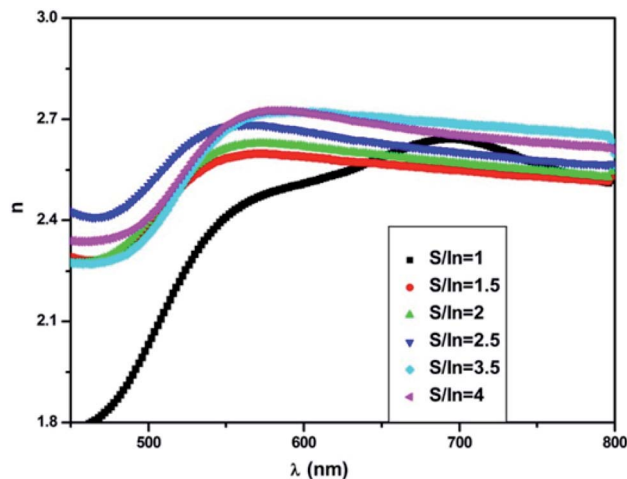
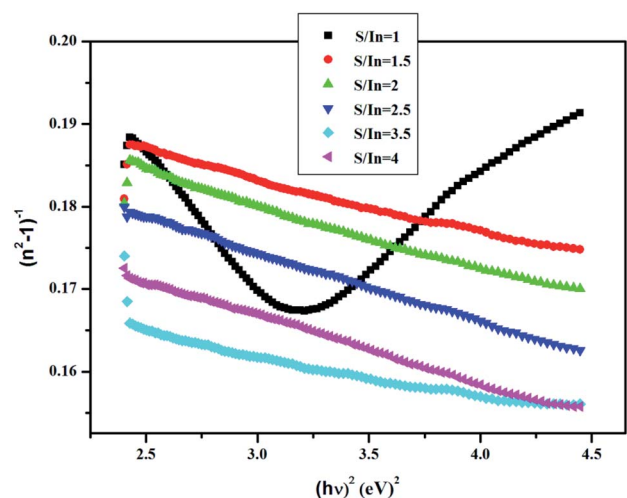
3.4.3. Refractive index. The refractive index (n) is given by:⁵³

$$n = (N + (N^2 - n_0^2 n_1^2)^{1/2})^{1/2} \quad (2)$$

Table 3 Calculated values of n , β and Cauchy parameters for different S/In molar ratios

S/In	n	B	C (μm^2)	β (eV)
1	2.40	3.14	−1.0	0.16
1.5	2.06	2.68	−0.3	0.29
2	2.10	2.73	−0.3	0.26
2.5	1.87	2.79	−0.4	0.27
3.5	2.11	2.81	−0.2	0.31
4	2.03	2.84	−0.4	0.26



Fig. 6 Spectral distribution of $n(\lambda)$ for different S/In molar ratios.Fig. 7 Plot of $(n^2 - 1)^{-1}$ versus $(h\nu)^2$.

$$N = \frac{2n_0n_1}{T_{\min}} - \frac{(n_0^2 + n_1^2)}{2} \quad (3)$$

where n_0 is the index of vacuum, n_1 is the glass substrate index and T_{\min} denotes minimum transmission.

The values of n are reported in Table 3. It can be observed that this value is minimum at S/In = 2.5, beyond this value it increases slightly. This is related to the variation in packing density of the films.⁵⁴

Fresnel equation⁵⁵ was used to evaluate the refractive index $n(\lambda)$ of the films as given by:

$$n = \left(\frac{1+R}{1-R} \right) + \sqrt{\frac{4R}{(1-R)^2} - k^2} \quad (4)$$

Fig. 6 displays the dispersion of n for different molar ratios. In the high absorption region, the refractive index increases strongly. The sharp onset of n at the absorption edge is

attributed to Van Hove singularity in the joint density state in the excitation of transition between two bands.⁵⁶ Thus, it follows the normal dispersion in the medium and weak absorption regions. This latter phenomenon is ascribed to both light scattering effect and absorbance decrease. From Fig. 6, it can be noticed that n varies from 2.4 to 2.75 with S/In ratio. The higher values of n make In_2S_3 thin films suitable for use in optoelectronic devices. Indeed, thin films are used for optical containment in waveguides, lasers and light-emitting diodes. The good value of n depends on the active layer used.

Thus, the increase of n indicates the better crystallinity of the films. Indeed, the material with amorphous nature has a low refractive index when compared to the polycrystalline one.⁵⁷

The variation of n along the Cauchy distribution is given by:⁵⁸

$$n = B + \frac{C}{\lambda^2} \quad (5)$$

where B and C denote the Cauchy's parameters.

Table 3 represents the values of these constants, which are evaluated from the fitting of $n(\lambda)$.

The dispersion energy was also calculated using the single oscillator model as described by Wemple and DiDomenico:⁵⁹

$$n^2 = 1 + \frac{E_0E_d}{E_0^2 - E^2} \quad (6)$$

where $E = h\nu$, E_0 is the oscillator energy and E_d is the dispersion energy.

Fig. 7 represents the linear variation of $(n^2 - 1)^{-1}$ versus $(h\nu)^2$ for these films. This permits us to determine both E_0 and E_d from the slope $(E_dE_0)^{-1}$ and (E_0/E_d) from the intercept at the origin for each straight line.

The results are listed in Table 4.

The highest dispersion energy value is obtained at S/In = 3.5, indicating that this film has a more ordered microstructure compared to the other films. The microstructure of In_2S_3 thin films varied with S/In ratio. Indeed, the influence of S/In molar ratio on microstructure is related with the nucleation and growth of In_2S_3 crystal.⁶⁰ Furthermore, sulfure deficiency or sulfur excess would involve the presence of impurities that can affect or destroy the microstructure.⁶¹

It can also be seen that the values of E_0 vary from 3.8 to 5.6 eV and oscillation energy describes the expressions $E_0 \approx 1.5E_g$ at S/In = 1 and $E_0 \approx 2E_g$ for S/In > 1. We can thus conclude that the Wemple–DiDomenico model describes well the behavior of these films.^{62,63} The lower value of ratio E_0 is obtained at S/In = 1, this could be attributed to the higher rate of diffusion of

Table 4 Evolution of optical parameters of In_2S_3 films with different S/In molar ratios

S/In	1	1.5	2	2.5	3.5	4
E_0 (eV)	3.8	5.6	5.1	4.9	5.4	4.8
E_d (eV)	15.5	27.8	25.3	25.5	30	25
E_g^{WDD} (eV)	1.9	2.8	2.5	2.4	2.7	2.4
ϵ_∞	9.6	7.5	7.8	7.4	8	7.9
ω_p (rad s ⁻¹)	14	8	9	10	8	10
N/m^* (m ⁻³)	6	1.5	2	2	1.5	2.4



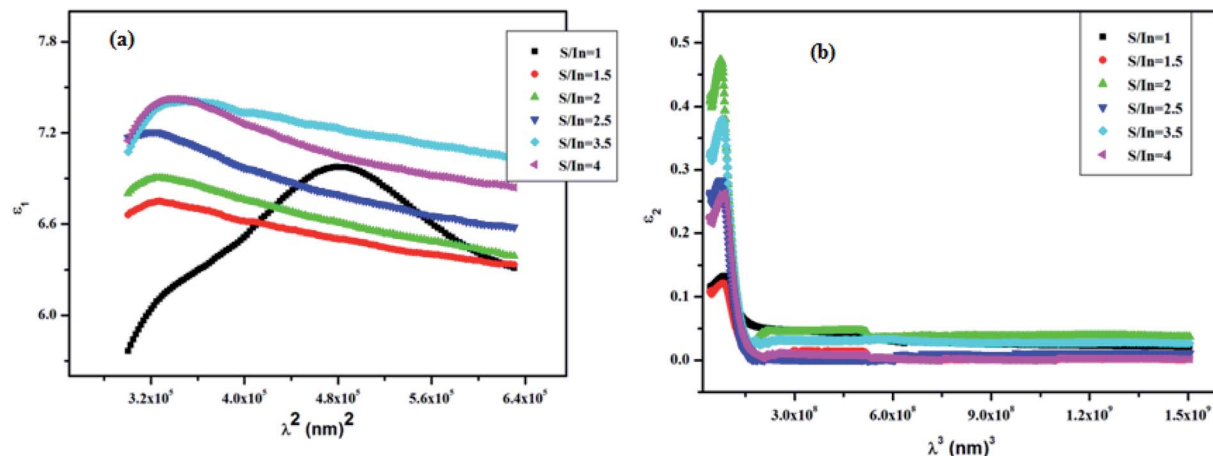


Fig. 8 (a) Plot of ϵ_1 versus λ^2 and (b) ϵ_2 versus λ^3 .

atoms in this film.⁶⁴ Furthermore, the change in the values of E_0 and E_d reveals that the molar ratio S/In is a suitable parameter for the change of refractive index and oscillator parameters. Thus, Tanaka⁶³ proposed the first approximate value of the optical band gap E_g^{WDD} from the Wemple–DiDomenico model using the expression ($E_g^{WDD} \approx \frac{E_0}{2}$). The E_g^{WDD} values are given in Table 4. The small difference between the two methods is ascribed to the calculations in two different regions. Indeed, in the case of Tauc method, the value of E_g is calculated in the absorption region of the spectrum, while in the Wemple–DiDomenico model the value of E_g^{WDD} is acquired in the transparent region of the spectrum.

The following empirical relation for E_d is established in crystals containing a single anion species:⁶⁵

$$E_d = \beta N_c Z_a N_c \quad (7)$$

where β is a constant, N_c and Z_a denote the coordination number of the nearest-neighbor cation and formal anion valency. N_c represents the effective number of valence electrons per anion. For In_2S_3 , N_c , Z_a and N_e , are equal to 6, 2 and 8, respectively. In addition, β takes two values: 0.26 ± 0.04 eV (ionic compound) and 0.37 ± 0.05 eV (covalent compound). In our work, the β values vary from 0.16 to 0.31 eV (Table 3). These

values agree with the first condition. Therefore, In_2S_3 films are found to be ionic compounds.

3.4.4. Dielectric constants. The real (ϵ_1) and imaginary parts (ϵ_2) of the dielectric constant are related to the wavelength (λ) by the formulas:⁶⁶

$$\epsilon_1 = \epsilon_\infty - \frac{\epsilon_\infty \omega_p^2}{4\pi^2 c^2} \lambda^2 \quad (8)$$

$$\epsilon_2 = -\frac{\epsilon_\infty \omega_p^2}{4\pi^3 c^3 \tau} \lambda^3 \quad (9)$$

The free carrier concentration-to-effective mass ratio can be obtained from the relation:

$$\omega_p^2 = \frac{4\pi N e^2}{\epsilon_\infty m_c^*} \quad (10)$$

where ϵ_∞ is infinite high frequency dielectric constant which is commonly associated with the free carriers and lattice vibration modes of the material dispersion properties,⁶⁷ τ , e , ω_p , and N/m_c^* denote respectively the relaxation time, electronic charge, plasma frequency and ratio of carrier concentration to the effective mass.

Fig. 8a and b, show that the behavior of ϵ_1 is similar to the refractive index (n). This is due to the smaller value of k compared to n . However, the behaviors of ϵ_2 and α are the same,

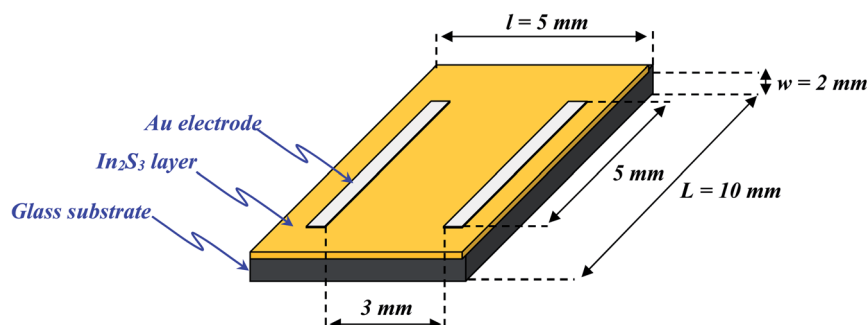


Fig. 9 Shape of In_2S_3 photodetector.



because ε_2 depends on the k values which are correlated to the variation of absorption coefficient (α). We observed high value of ε_1 at low wavelengths; this is due to the presence of space charge polarization at the grain boundaries, which generates a potential barrier. Thus, a charge accumulation at the grain boundary occurred, which leads to highest value of ε_1 .⁶⁸ However, the real part decreases with the increase of wavelength. This trend is due to the reduction of space charge polarization effect.

From the intercepts and slopes of the ε_1 plots as a function of λ^2 (see Fig. 8a), the values of ε_∞ and N/m^* for the films are estimated and reported in Table 4.

The increase in refractive index induces a rise in the electromagnetic radiation absorption which in turn increases the frequency. In addition, the value of n becomes high when the radiation frequency corresponds to the electron characteristic frequency. The physical interpretation of the variation of plasma frequency can be ascribed to the variation of the concentration of the charged carriers in In_2S_3 thin films. Hence, the high value of ω_p at $S/\text{In} = 1$ might be due to the higher concentration of the charged carriers in this film. This finding confirms the results of optical band gap value at $S/\text{In} = 1$. As can be seen, all N/m^* values are of the order of 10^{19} m^{-3} . Bouguila *et al.*⁶⁹ reported comparable values for In_2S_3 thin films for different thicknesses. The higher value obtained at $S/\text{In} = 1$, could be explained by higher defect states in the film.⁷⁰ Besides, Nicholas *et al.*⁷¹ reported that the low value of effective mass leads to high carrier mobility. Thus, it is clear from Table 2 that the values of N/m^* are affected by the S/In molar ratio. So, we can say that ε_∞ and N/m^* are assigned to the internal microstructure.⁷²

4. Photoresponse

Due to absorption in the UV and visible region, In_2S_3 is considered here as photodetector. To study the photoresponse of the In_2S_3 film ($S/\text{In} = 2$), two rectangular gold electrodes

3 mm long and 3 mm apart were deposited on the film using thermal evaporation technique under high vacuum. The samples obtained have the shape of a parallelepiped, the dimensions of the glass substrate are ($L = 10 \text{ mm}$, $l = 5 \text{ mm}$, $w = 2 \text{ mm}$) and the In_2S_3 film thickness is around $2 \mu\text{m}$ (Fig. 9).

I - V characteristics measured in dark and under illumination by neon lamp with a bias voltage ranging from -10 to 10 volts are shown in Fig. 10a. The linear I - V curves from the sample confirm the ohmic nature of $\text{Au}/\text{In}_2\text{S}_3$ contacts. This ohmic contact with Au electrodes enables excellent photo-response behaviors. Furthermore, the formation of ohmic contacts between semiconductors and metals serving as electrodes is an important requirement for photodetector device. Indeed, this contact is required to inject the maximum current density across the contact.⁷³

The resistance evolution was measured, while the sample was illuminated by reversible switching (ON/OFF) cycles of the neon lamp. The light was ON for 15 min and OFF for 15 min for all cycles. Fig. 10b shows that the resistance of In_2S_3 film increases in dark until reaching its equilibrium value and decreases quickly to the baseline value in light. We also observe that repetitive cycles profile reveals the ability of the material to produce the same response, by exhibiting an acceptable reproducibility and reversibility of the response. This evolution suggests that more photons with higher energy are involved in the photon-induced charge-transfer process. This behavior is suitable given the fact that typical absorption is located for wavelength $< 500 \text{ nm}$, as shown in Fig. 5. Likewise, the optical excitation allows the generation of electron-hole pairs. The fact that the transit time of the holes is much greater than that of the electrons; a single hole can cause the circulation of several electrons in order to ensure the electrical neutrality of the material, which enhances photocurrent response.⁷⁴

The increase of photocurrent is traduced by the decrease of the resistance. In this context, we have adjusted in Fig. 10b, the resistance curves *versus* time with a bi-exponential equations that have two evolution components in both decaying and rising progress.⁷⁴

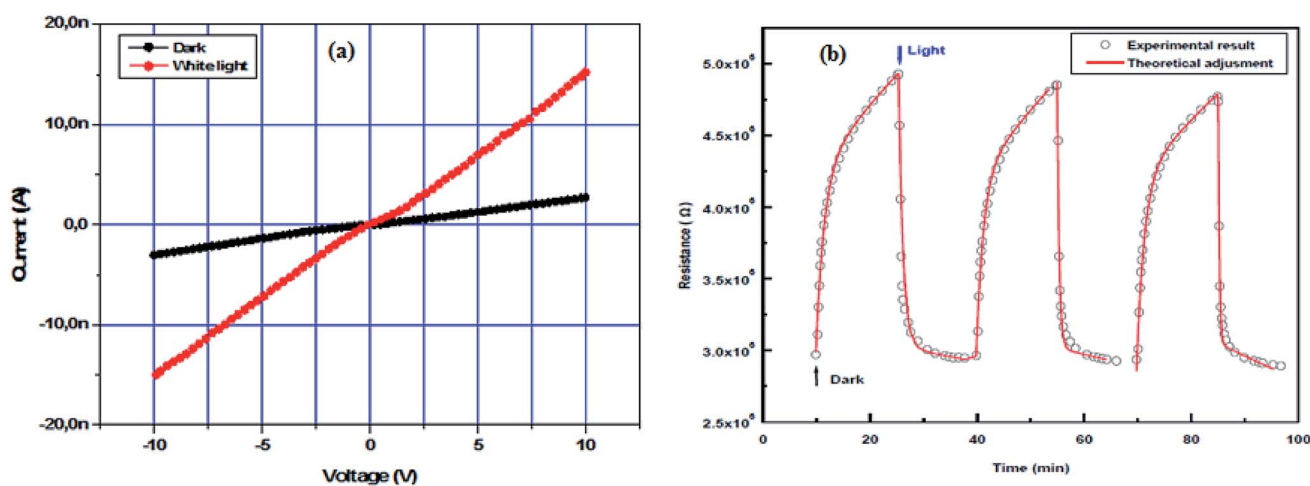


Fig. 10 (a) I - V characteristics of In_2S_3 thin film in dark and under illumination, (b) adjustment of In_2S_3 thin film photoresponse with two exponentials evolutions.



Table 5 Theoretical values of time constants for first and second kinetics of photocurrent cycles

Cycle number	Light		Dark	
	τ_1 (s)	τ_2 (s)	τ_1 (s)	τ_2 (s)
1	48	24 877	90	4361
2	22	20 362	77	4194
3	14	10 223	84	4695

$$r_{\text{light}} = A_1 e^{-\frac{t}{\tau_1}} + A_2 e^{-\frac{t}{\tau_2}} \quad (11)$$

$$r_{\text{dark}} = A_1 \left(1 - e^{-\frac{t}{\tau_1}}\right) + A_2 \left(1 - e^{-\frac{t}{\tau_2}}\right) \quad (12)$$

where τ_1 and τ_2 are the time constants for first and second kinetics of photocurrent cycles, respectively.

The determination of the constants A_1 , A_2 , τ_1 and τ_2 is not obvious given the nonlinearity of the eqn (11) and (12). As a result, we divide each film response into two parts:

-the first part is dominated by the fast kinetic (τ_1) and corresponds to a significant variation of the resistance.

-the second part is dominated by a slow kinetic (τ_2) and results in a weak variation of the resistance.

We have adjusted the last points of the second domain ($t \gg \tau_1$) by the function $A_2 e^{-t/\tau_2}$ and we have deduced A_2 and τ_2 values using the least squares method. Then, the quantity $A_2 e^{-t/\tau_2}$ is subtracted from the experimental points of the first domain ($0 < t < \tau_1$). The obtained results are similarly adjusted *via* the same technique to determine A_1 and τ_1 . Several iterations were made in order to adjust precisely the theoretical fit with the experimental results. The fit is constructed correspond to the theoretical function. The τ_1 and τ_2 values are regrouped in Table 5.

The results of the theoretical adjustment demonstrate good conformity with the experimental data. The evolution of the resistance under illumination and in dark follows two kinetics: the first is fast, the other is slow. For the fast kinetic, the averages values of τ_1 are found around 28 s in light and 84 s in dark. We can note that time constants associated in light are relatively small compared to those associated with other in dark. This result is expected because the charge carrier generation time is shorter than the recombination time.⁷⁵

5. Conclusion

Using spray pyrolysis technique, we have deposited In_2S_3 thin films on a glass substrate at different S/In ratios. We investigated the influence of S/In molar ratios on their structural, morphological and optical properties. The Raman analysis confirms the absence of secondary phase. The RMS roughness decreases from 20 to 6 nm as the molar ratio increases. The PL study shows the presence of two major emission bands. In addition, n of the films is shown to be dependent on the S/In ratio. The dispersion of the layers is investigated using the Wemple–DiDomenico model. The oscillator energies (E_0 , E_d) are deduced. E_0 can be related to E_g in close approximation by $E_0 \approx$

$1.5E_g$ at $S/\text{In} = 1$ and $E_0 \approx 2E_g$ for $S/\text{In} > 1$. Furthermore, the calculated value of β shows that In_2S_3 is an ionic compound. The photoconductive property, the optical transmission and energy gap make it a promising material for optoelectronics applications.

Data availability statement

The data that support the findings of this study are available from the corresponding author upon reasonable request.

Conflicts of interest

There are no conflicts to declare.

Acknowledgements

This work was supported by Tunisian Ministry of Higher Education and Scientific Research, Spanish Ministry of Science and Innovation – FEDER Funds (MODENA Project CTQ2016-79461-R) and Fundación Ramón Areces (Spain, Project CIVP18A3940). NANOMAG group belongs to Galician Competitive Research Group ED431C-2017/22, programme co-funded by FEDER, and AEMAT Strategic Partnership (ED431E-2018/08, Xunta de Galicia, Spain). The authors are grateful to Professor Ibrahim Halidou (Faculté des Sciences et Techniques, Université Abdou Moumouni, Niamey, Niger) for his revision of the manuscript.

References

- W. Yue, F. Wei, Y. Li, L. Zhang, Q. Zhang, Q. Qiao and H. Qiao, *Mater. Sci. Semicond. Process.*, 2018, **76**, 14–24.
- W. Yue, F. Wu, C. Liu, Z. Qiu, Q. Cui, H. Zhang, F. Gao, W. Shen, Q. Qiao and M. Wang, *Sol. Energy Mater. Sol. Cells*, 2013, **114**, 43–53.
- H. Chen, W. Fu, H. Yang, P. Sun, Y. Zhang, L. Wang, W. Zhao, X. Zhou, H. Zhao, Q. Jing, X. Qi and Y. Li, *Electrochim. Acta*, 2010, **56**, 919–924.
- D. Ma, J. Zai, Y. Wang, Q. Qiao and X. Qian, *ChemNanoMat*, 2018, **4**(10), 1043–1047.
- F. Wu, R. Pathak, L. Jiang, W. Chen, C. Chen, Y. Tong, T. Zhang, R. Jian and Q. Qiao, *Nanoscale Res. Lett.*, 2019, **14**, 1–10.
- K. M. Hynes and J. Newham, *Proceedings 16th European Photovoltaic Solar Energy Conference*, 2000, p. 2297.
- D. Braunger, D. Hariskos, T. Walter and H. W. Shock, *Sol. Energy Mater. Sol. Cells*, 1997, **40**, 97.
- W. Rehwald and G. Harbeke, *J. Phys. Chem. Solids*, 1965, **26**, 1309–1318.
- Y. Osman, M. Fedawy, M. Abaza and M. H. Aly, *J. Phys.*, 2020, **1447**, 012057.
- R. H. Bube and W. H. Mc Carroll, *J. Phys. Chem. Solids*, 1959, **10**, 333.
- T. John, S. Bini, Y. Kashiwaba, T. Abe, Y. Yasuhiro, C. S. Kartha and K. P. Vijayakamur, *Semicond. Sci. Technol.*, 2003, **18**, 491.



- 12 S. S. Wang, F. J. Shiou, C. C. Tsao, S. W. Huang and C. Y. Hsu, *Mater. Sci. Semicond. Process.*, 2013, **16**, 1879.
- 13 J. Feng, H. Zhu and X. Yang, *Nanoscale*, 2013, **5**, 6318.
- 14 S. Peng, L. Li, Y. Wu, L. Jia, L. Tian, M. Srinivasan, S. Ramakrishna, Q. Yan and S. G. Mhaisalkar, *CrystEngComm*, 2013, **15**, 1922–1930.
- 15 X. Xie and G. Shen, *Nanoscale*, 2015, **7**, 5046–5052.
- 16 R. Souissi, N. Bouguila and A. Labidi, *Sens. Actuators, B*, 2018, **261**, 522–530.
- 17 R. Xu, H. Li, W. Zhang, Z. Yang, G. Liu, Z. Xu, H. Shao and G. Qiao, *Phys. Chem. Chem. Phys.*, 2016, **18**, 2710–2717.
- 18 W. T. Kim and C. D. Kim, *J. Appl. Phys.*, 1986, **60**, 2631–2633.
- 19 N. A. Allsop, A. Schönmann, A. Belaidi, H. J. Muffler, B. Mertesacker, W. Bohne, E. Strub, J. Röhrich, M. C. Lux-Steiner and C. H. Fischer, *Thin Solid Films*, 2006, **513**, 52–56.
- 20 C. H. Ho, Y. P. Wang and Y. S. Huang, *Appl. Phys. Lett.*, 2012, **100**, 131905–131909.
- 21 R. S. Beker, T. Zheng, J. Elton, M. Bai and M. Saeki, *Sol. Energy Mater.*, 1986, **13**, 97–107.
- 22 M. Mathew, R. Jayakrishnan, P. M. R. Kumar, C. S. Kartha, K. P. Vijayakumar, Y. Kashiwaba and T. Abe, *J. Appl. Phys.*, 2006, **100**, 033504.
- 23 N. Bouguila, M. Kraini, I. Najeh, I. Halidou, E. Lacaze, H. Bouchriha, H. Bouzouita and S. Alaya, *J. Electron. Mater.*, 2015, **44**, 4213–4219.
- 24 K. Otto, A. Katerski, A. Mere, O. Volobujeva and M. Krunks, *Thin Solid Films*, 2011, **519**, 3055–3060.
- 25 N. Barreau, *Sol. Energy*, 2009, **83**, 363–371.
- 26 A. Akkari, C. Guasch, M. Castagne and N. K. Turki, *Mater. Sci.*, 2011, **46**, 6285–6292.
- 27 B. Asenjo, C. Sanz, C. Guillén, A. M. Chaparro, M. T. Gutiérrez and J. Herrero, *Thin Solid Films*, 2007, **515**, 6041–6044.
- 28 A. Timoumi, H. Bouzouita and B. Rezig, *Thin Solid Films*, 2011, **519**, 7615–7619.
- 29 S. Sigdel, A. Dubey, H. Elbohy, A. Aboagye, D. Galipeau, L. Zhang, H. Fongc and Q. Qiao, *J. Mater. Chem. A*, 2014, **2**, 11448–11453.
- 30 E. Ngo, S. Venkatesan, D. Galipeau and Q. Qiao, *IEEE Trans. Electron. Dev.*, 2013, **60**, 2372–2378.
- 31 N. Bouguila, H. Bouzouita, E. Lacaze, A. Belhadj Amara, H. Bouchriha and A. Dhoubi, *J. Phys. III*, 1997, **7**, 1647–1660.
- 32 N. Jebbari, F. Saadallah, C. Guasch, N. K. Turki, N. Yacoubi and R. Bennaceur, *Appl. Phys. A*, 2014, **116**, 2011–2017.
- 33 S. Elfarrass, B. Hartiti, A. Ridah and P. Thevenin, *J. Mater. Environ. Sci.*, 2015, **6**, 487–490.
- 34 M. Calixto-Rodriguez, A. Tiburcio-Silver, A. Ortiz and A. Sanchez-Juarez, *Thin Solid Films*, 2005, **480**, 133–137.
- 35 S. Buecheler, D. Corica, D. Guettler, A. Chirila, R. Verma, U. Müller, T. P. Niesen, J. Palm and A. N. Tiwari, *Thin Solid Films*, 2009, **517**, 2312–2315.
- 36 T. T. John, C. S. Kartha and K. P. Vijayakumar, *Appl. Surf. Sci.*, 2005, **252**, 1360–1367.
- 37 X. Zhang, H. Wang, J. Xu, L. Yang and M. Ren, *Key Eng. Mater.*, 2011, **474–476**, 988–1001.
- 38 L. Bhira, G. Gouturier, J. Salardenne, N. Barreau and J. C. Bernede, *Phys. Status Solidi*, 2000, **181**, 427.
- 39 K. Kambas, J. Spyridelis and M. Balkanski, *Phys. Status Solidi*, 1981, **105**, 291.
- 40 H. Tao, H. Zang, G. Dong, J. Zeng and X. Zhao, *Optoelectron. Adv. Mater. Rapid Commun.*, 2008, **2**, 356–359.
- 41 M. Kraini, N. Bouguila, I. Halidou, A. Moadhen, C. Vázquez-Vázquez, M. A. López Quintela and S. Alaya, *J. Electron. Mater.*, 2015, **44**, 2536.
- 42 Y. Xiong, Y. Xie, G. Du, X. Tian and Y. Qian, *J. Solid State Chem.*, 2002, **166**, 336.
- 43 J. Yaxin, O. Yufeng, Y. Zhou, Y. Yong, W. Dan, Y. Chuanpeng, L. Lian, Z. Yong and Y. Zhao, *Surf. Coat. Technol.*, 2015, **276**, 587.
- 44 N. Bouguila, A. Timoumi, H. Bouzouita, E. Lacaze, H. Bouchriha and B. Rezig, *Eur. Phys. J. Appl. Phys.*, 2013, **63**, 20301.
- 45 M. S. Eluyemi, M. A. Eleruja, A. V. Adedeji, B. Olofinjana, O. Fasakin, O. O. Akinwunmi, O. O. Ilori, A. T. Famojuro, S. A. Ayinde and E. O. B. Ajayi, *Graphene*, 2016, **5**, 143–154.
- 46 C. Tapia, S. P. Berglund, D. Friedrich, T. Dittrich, P. Bogdanoff, Y. Liu, S. Levchenko, T. Unold, J. C. Conesa, A. L. De Lacey, M. Pita and S. Fiechter, *J. Phys. Chem.*, 2016, **120**, 28753.
- 47 C. H. Ho, Y. P. Wang, C. H. Chan, Y. S. Huang and C. H. Li, *J. Appl. Phys.*, 2010, **108**, 043518.
- 48 T. T. John, C. S. Kartha, K. P. Vijayakumar, T. Abe and Y. Kashiwaba, *Appl. Surf. Sci.*, 2005, **252**, 1360.
- 49 R. Jayakrishnan, T. T. John, C. S. Kartha, K. P. Vijayakumar, D. Jain, L. S. Sharath Chandra and V. Ganesan, *J. Appl. Phys.*, 2008, **103**, 053106.
- 50 M. Ajili and N. Turki Kamoun, *J. Mater. Sci.: Mater. Electron.*, 2014, **25**, 3840–3845.
- 51 Y. C. Liu, S. K. Tung and J. H. Hsieh, *J. Cryst. Growth*, 2006, **287**, 105–111.
- 52 L. Ling-Yan, Y. Jin-Ling, C. Shu-Ying and L. Pei-Min, *Chin. Phys. B*, 2015, **24**, 078103.
- 53 R. Swanepoel, *J. Phys. E Sci. Instrum.*, 1983, **16**, 1214–1222.
- 54 M. M. El-Nahass, B. A. Khalifa, H. S. Soliman and M. A. M. Seyam, *Thin Solid Films*, 2006, **515**, 1796–1801.
- 55 N. Revathi, P. Prathap, Y. P. V. Subbaiah and K. T. R. Reddy, *J. Phys. D Appl. Phys.*, 2008, **41**, 155404–155413.
- 56 G. F. Bassani and G. P. Parravini, *Electronic States and Optical Transitions in Solids*, Pergamon Press, Oxford, 1989.
- 57 L. J. Meng, J. Gao, M. P. dos Santos, X. Wang and T. Wang, *Thin Solid Films*, 2008, **516**, 1365–1369.
- 58 H. G. Tompkins and W. A. McGahan, *Spectroscopic Ellipsometry and Reflectometry: A user's guide*, New York, Wiley, 1999.
- 59 S. H. Wemple and M. DiDomenico, *Phys. Rev. B: Solid State*, 1971, **3**, 1338–1351.
- 60 W. Li, P. Liu, K. Zhang, F. Ma, X. Liu, X. Chen and D. He, *Integr. Ferroelectr.*, 2017, **180**, 12–23.
- 61 A. Richardt and A. M. Durand, *Le vide – Les Couches Minces, Les Couches Dures*, Editions in Fine, Paris, 1994, p. 20301.
- 62 A. Timoumi, H. Bouzouita and B. Rezig, *J. Basic Appl. Sci.*, 2013, **7**, 448–456.
- 63 K. Tanaka, *Thin Solid Films*, 1980, **66**, 271–279.



- 64 A. El-Alwany, O. M. Samir, M. A. Algradee, M. M. Hafith and M. A. Ab-Rahim, *Condens. Matter Phys.*, 2015, **5**, 220–231.
- 65 S. Goldsmith, E. Çetinörgü and R. L. Boxman, *Thin Solid Films*, 2009, **517**, 5146–5150.
- 66 A. Mhamdi, B. Ouni, A. Amlouk, K. Boubaker and M. Amlouk, *J. Alloys Compd.*, 2014, **582**, 810–822.
- 67 S. A. Mahmoud, S. Alshomer and M. A. Tarawnh, *Mod. Phys.*, 2011, **2**, 1178–1186.
- 68 M. Abdullah Dar, K. Majid, K. Mijasam Bato and R. K. Kotnala, *J. Alloys Compd.*, 2015, **632**, 307–320.
- 69 N. Bouguila, M. Kraini, I. Halidou, E. Lacaze, H. Bouchriha and H. Bouzouita, *J. Electron. Mater.*, 2015, **45**, 829–838.
- 70 R. L. Z. Hoye, K. P. Musselman and J. L. M. Driscoll, *Apl. Mat.*, 2013, **1**, 060701, DOI: 10.1063/1.4833475.
- 71 R. J. Nicholas, J. C. Portal, C. Houlbert, P. Perrier and T. P. Pearsall, *Appl. Phys. Lett.*, 1979, **34**, 492–494.
- 72 G. A. Mohamed, E. M. Mohamed and A. Abu El-Fadl, *Phys. B*, 2001, **308–310**, 949–953.
- 73 Y. Hou, X. Du, S. Scheiner, D. P. McMeekin, Z. Wang, N. Li, M. S. Killian, H. Chen, M. Richter, I. Levchuk, N. Schrenker, E. Spiecker, T. Stubhan, N. A. Luechinger, A. Hirsch, P. Schmuki, H. P. Steinrück, R. H. Fink, M. Halik, H. J. Snaith and C. J. Brabec, *Science*, 2017, **358**, 1192–1197.
- 74 H. Cansizoglu, M. F. Cansizoglu, F. Watanabe and T. Karabacak, *ACS Appl. Mater. Interfaces*, 2014, **6**, 8673–8682.
- 75 S. Ghosh, M. Saha, V. Dev Ashok, A. Chatterjee and S. K. De, *Nanotechnology*, 2016, **27**, 155708–155724.

